ACS APPLIED MATERIALS & INTERFACES

Research Article

www.acsami.org

Redox-Induced Enhancement in Interfacial Capacitance of the Titania Nanotube/Bismuth Oxide Composite Electrode

Biplab Sarma,[†] Abraham L. Jurovitzki,[†] York R. Smith,[†] Swomitra K. Mohanty,[‡] and Mano Misra*[,†,‡]

[†]Metallurgical Engineering, University of Utah, Salt Lake City, Utah 84112, United States

[‡]Chemical Engineering, University of Utah, Salt Lake City, Utah 84112, United States

Supporting Information

ABSTRACT: Bismuth oxide (Bi_2O_3) decorated titania nanotube array (T-NT) composite materials were synthesized by a simple, yet versatile electrodeposition method. The effects of deposition current density and time on morphology evolution of the bismuth oxide phase were analyzed. It was found that an optimum deposition condition in terms of current density and time could be reached to achieve uniform and equiaxed crystal morphology of the deposited oxide phase. The morphology, shape, size distribution, and crystal structure of the bismuth oxide phase were evaluated using scanning electron microscopy (SEM), X-ray diffraction (XRD), X-ray photoelectron spectroscopy (XPS), and Raman spectroscopic techniques. The electrochemical capacitance of the T-NT/Bi_2O_3 composites was studied by conducting cyclic voltammetry and galvanostatic charge−discharge experiments. These studies indicated that the capacitance behavior of the composite material was dependent on the morphology and distribution of the bismuth oxide phase. The capacitance was greatly enhanced for the composite having equiaxed and uniformly distributed bismuth oxide particles. The maximum interfacial capacitance achieved in this study was approximately 430 mF cm^{-2}. Galvanostatic charge−discharge experiments conducted on the composite materials suggested stable capacitance behavior together with excellent capacitance retention even after 500 cycles of continuous charge−discharge operation.

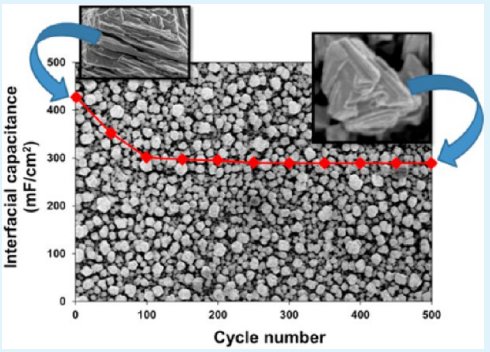

KEYWORDS: *bismuth oxide (Bi_2O_3), TiO_2 nanotube arrays, electrochemical capacitor, anodization, pseudocapacitor, electrodeposition*

1. INTRODUCTION

Electrochemical capacitors are attractive energy storage devices because of their high power and energy densities, together with long cycle life.[1,2] They are classified into two main categories, namely, (i) electric double layer (EDL) capacitor and (ii) redox capacitor (also known as pseudocapacitor).[3] The second type of capacitor, i.e., redox capacitor, derives its power/energy from the rapid and reversible faradic reactions that take place on the electrode surface in contact with the electrolyte. As transition metal oxides exhibit several oxidation states/structures, special interest had been bestowed to evaluate several of these oxides as supercapacitors. Among them, hydrous ruthenium oxide, iridium oxide, nickel oxide, manganese oxide, and cobalt oxide have been the most commonly studied thus far.[2,4−7] Various synthesis methods such as electrodeposition,[8] template-based growth,[9,10] immersion,[11] chemical precipitation,[12] etc. had been adapted to prepared such oxide materials for supercapacitor applications.

Recently, titania nanotubular arrays (T-NTs), synthesized via the electrochemical anodization method, have received immense interest for various applications such as a deposition support for various metals.[3,13−15] T-NTs have high surface area, have good chemical stability, and are nontoxic in nature.[16−19] Moreover, the electrochemical anodization method is a simple technique which can be employed to synthesize nanotubular structures with high control. By controlling the anodization potential and the electrolyte bath chemistry, various geometries in terms of pore diameter and tube length of T-NT can be fabricated. Composite materials consisting of the T-NT substrate decorated with transition metal oxides have been studied for their electrochemical capacitance.[3,13] For example, fabrication of the T-NT/NiO composite electrode using the electrodeposition method produced interfacial capacitance of 128 mF cm^{-2}.[3] The authors suggested that the highly ordered architecture and high surface area of the T-NT substrate facilitated enhanced reaction sites as well as improved charge and mass transfer through the tubular tunnels, thereby increasing the capacitance of the composite structure.

Bismuth oxide is an attractive transition metal oxide due to its large energy band gap, good oxygen-ion conductivity, high refractive index, and dielectric permittivity.[20] Additionally, bismuth oxide is nontoxic and biocompatible.[21] Therefore, bismuth oxide has been studied for several applications such as: catalyst, optical materials, electrochemical capacitors, gas

Received: November 17, 2012
Accepted: February 17, 2013
Published: February 17, 2013

sensors, biosensor, and solid oxide fuel cells.[22] In the field of electrochemical capacitors, bismuth oxide has shown superior properties in terms of specific capacitance and durability in long charge−discharge cycle operations.[20] Despite this, bismuth oxide has not been studied in depth for their capacitance behavior, and only a few reports are available.[20−26] The first capacitance research was performed by Gujar and co-workers.[20] In their study, they synthesized a Cu/Bi_2O_3 composite material by electrodeposition of the oxide onto a copper substrate. The composite thus formed exhibited a specific capacitance of 98 F g^{-1}. In subsequent studies,[23−27] researchers have developed better composite structures in terms of a more porous substrate/supporting material with Bi_2O_3 to obtain higher specific capacitance. For example, a composite structure consisting of highly ordered mesoporous carbon (HOMC) and Bi_2O_3, fabricated by Yuan et al.,[24] showed relatively higher specific capacitance of 180 F g^{-1}. A further increase in specific capacitance was recently reported through a composite architecture of graphene/Bi_2O_3.[25] The authors in this study argued that the use of porous graphene as the supporting material enhanced the capacitance of the graphene/Bi_2O_3 composite. This is partly because of the porous substrates with large surface area facilitating improved interfacial ions and charge transfer compared to that of a solid and/or bulk substrate. However, synthesis of porous graphene is rather costly and time consuming and requires multiple steps to reach the final component as composite material.[25] In a study conducted by Murugesan et al.,[26] a bismuth-rich oxide phase was synthesized over T-NT using a hydrothermal method. This material demonstrated enhanced photoelectrochemical performance over plain T-NT.

In this study, we have demonstrated a simple electrodeposition method of depositing Bi_2O_3 onto a T-NT substrate to fabricate T-NT/Bi_2O_3 composite materials. The composite materials formed were tested for their supercapacitance application by conducting various electrochemical tests, such as cyclic voltammetry (CV) and galvanostatic charge−discharge. The interfacial capacitance obtained for the T-NT/Bi_2O_3 materials has been explained in relation to deposited morphology and compared with the previously reported capacitance values for various other electrode materials.

2. EXPERIMENTAL SECTION

2.1. Sample Preparation. Ti samples (10 mm × 15 mm × 0.1 mm) were extracted from a titanium foil for anodization. The samples were polished and subsequently degreased in a 50/50 (vol %) solution of acetone and isopropyl alcohol for 15 min by sonication. Afterwards, the coupons were dried under a stream of air at 100 °C.

2.2. Potentiostatic Anodization. T-NT substrates were prepared by potentiostatic anodization. The anodization electrolyte consisted of ethylene glycol (EG), 0.5 wt % ammonium fluoride, and 10 wt % H_2O. The electrolyte was aged for at least 48 h in a sealed container prior to anodization. Anodization was carried out with a DC power source (Agilent Technologies E3647A) connected to a titanium coupon (anode) and platinum (cathode). The electrolyte was stirred at 90 rpm. The anodization was carried out at a constant voltage of 40 V for one hour at room temperature. Immediately after the anodization, the titanium coupon was removed and cleaned by sonication for 3−5 seconds in de-ionized water and dried at 100 °C for one hour in air.

2.3. TiO_2 NT Annealing. Annealing was performed in a muffle furnace in air at 500 °C. The temperature was raised at a rate of 1.5 °C/min to the set point and maintained for 2 h. After holding the anodized sample at the elevated temperature, the samples were allowed to cool within the furnace by natural convection.

2.4. Electrochemical Deposition. Electrochemical deposition was performed using a potentiostat (Gamry Reference 600) connected to a three-electrode setup with anodized T-NT sample as the working electrode, platinum coil as the counter electrode, and saturated Ag/AgCl (3 M) as a reference electrode. Bi_2O_3 was deposited by performing galvanostatic deposition at room temperature in an aqueous solution of 10 mM bismuth nitrate ($Bi(NO_3)_3$), 0.1 M tartartic acid ($HOCO(CHOH)_2COOH$), and 3 M sodium hydroxide (NaOH). Deposition was performed at various current densities (−1, −3, −5, and −10 mA cm^{-2}) for 15 min. Also, a set of depositions was carried out at a constant current density of −5 mA cm^{-2} for various periods of time ranging from 5 to 60 min. The deposition bath was constantly stirred at 170 rpm during experiments.

2.5. Characterization. Examination of the morphology (surface and cross section) for the T-NT and T-NT/Bi_2O_3 composites was performed using a field emission scanning electron microscope (Hitachi S-4800). X-ray diffraction (SIEMENS D5000) was utilized to determine the crystal phases present. The diffractometer used Cu Kα radiation, and the scan was performed from 25° to 75°. Raman spectroscopy was carried out by using an R 3000 QE portable Raman spectrometer (made by Raman Systems) equipped with a 785 nm laser (power of ∼140 mW) used for excitation. The Raman spectrometer provides wavelength stability of less than 1 cm^{-1} drift for over a 12 h period. The Raman results are available in the Supporting Information. An X-ray photoelectron spectroscopy (XPS) study was carried out using monochromatic Al Kα source (PE = 1600 eV) on a Kratos Axis Ultra DLD instrument, with a 300−700 μm spot size. Dwell time was set to 200 ms with three sweeps and a step size of 1 eV (0.1 eV for regional scans).

2.6. Electrochemical Measurements. The electrochemical properties of the T-NT/Bi_2O_3 samples were tested using a potentiostat (Gamry Reference 600), connected to a three-electrode setup consisting of the T-NT/Bi_2O_3 sample as the working electrode, platinum coil as the counter electrode, and a saturated Ag/AgCl electrode as a reference electrode. Electrochemical measurements were performed at room temperature. Cyclic voltammetry (CV) tests and galvanostatic charge/discharge tests were performed in an aqueous solution of 1 M NaOH using this setup.

3. RESULTS AND DISCUSSION

Figure 1 shows the self-organized and vertically aligned compact T-NT array structure formed on the titanium foil by

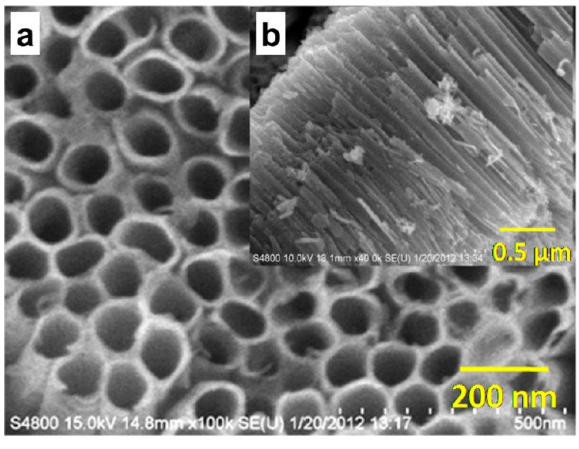

Figure 1. Top (a) and cross-sectional (b) view of T-NT formed by anodization at 40 V for 1 h.

anodization at 40 V for 1 h. The nanotubes were found to have an average diameter of approximately 90 nm, length of approximately 1.5 μm, and wall thicknesses in the range of 15−20 nm. To establish suitable deposition parameters for Bi_2O_3 on the T-NT substrate, CV studies were carried out in an

aqueous solution containing 10 mM bismuth nitrate, 0.1 M tartaric acid, and 3 M sodium hydroxide. The resultant CV profile, scanned at 20 mV s^{-1} between 0 and −1 V vs the Ag/AgCl reference electrode, is shown in Figure 2. The reduction

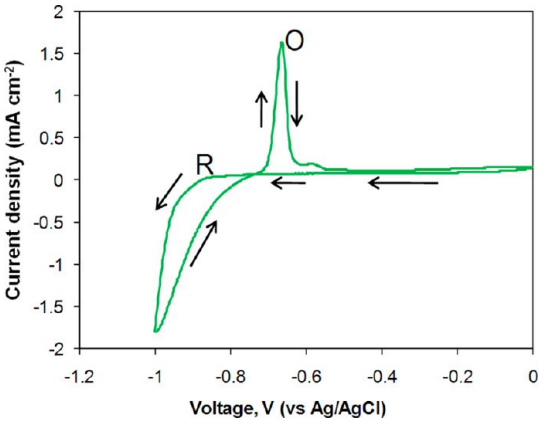

Figure 2. Cyclic voltammetry of the T-NT substrate in aqueous solution of 10 mM bismuth nitrate, 0.1 M tartartic acid, and 3 M sodium hydroxide at 20 mV s^{-1} scan rate. The start of reduction and the peak for oxidation are marked as 'R' and 'O', respectively.

and oxidation peaks are marked as 'R' and 'O' during the forward and reverse directions of the scan, respectively. It appears that the reduction started at a potential below −0.87 V, and the oxidation process peaked at about −0.67 V. In the high pH (~14) solution, the Bi_2O_3 is reported to form through the following reactions[20]

$$Bi^{3+} + 2OH^- \rightarrow Bi(OH)_2^+ \quad (1)$$

$$2Bi(OH)_2^+ + 2OH^- \rightarrow Bi_2O_3 + 3H_2O \quad (2)$$

The $Bi(OH)_2^+$ is formed due to the highly alkaline nature of the solution by the reaction in eq 1. The positively charged bismuth hydroxide ions ($Bi(OH)_2^+$) further react with the hydroxyl ions to form Bi_2O_3 following reaction in eq 2 on the cathode at approximately −0.87 V or lower as shown in the CV profile.

The morphology of the Bi_2O_3 deposit on the T-NT substrate at various deposition current densities and times was examined using SEM. Generally, the morphological aspects of the electrodeposit can easily be manipulated by changing the deposition parameters, such as current density, deposition time, potential, pH, concentration, and temperature of the solution bath.[2] Figure 3 shows the SEM micrographs of the Bi_2O_3 deposits obtained after 15 min of deposition at current densities (i) of −1, −3, −5, and −10 mA cm^{-2}. During deposition, the steady state potentials changed from −0.88 to −1.08 V upon an increase in current density from −1 to −10 mA cm^{-2}, which appeared to be consistent with the CV analysis (Figure 2). The general morphology of the deposits appeared to be crystallites with ragged edges as shown in the magnified images (Figure 3(a′−d″)). A few important points can be noted by comparing the nature of deposits obtained at various current densities. With increasing i, the size and distribution behavior of the Bi_2O_3 deposits changed. For example, the average sizes (length) of the oxide crystals obtained at i = −1 mA cm^{-2} were in the range of 0.7−2 μm, while the size increased to about 1−3 μm at i = −5 mA cm^{-2} (Figure 3a′ and c′). Furthermore, at a relatively lower current density of i = −1 mA cm^{-2}, the deposition was relatively nonuniform throughout the substrate (Figure 3a). However, the oxide phase appeared to be uniformly distributed at higher current densities (Figure 3 b,c). It is interesting to note that the oxide crystals became more equiaxed when deposition was carried out at i = −5 mA cm^{-2}. Because of this morphology, the oxide layer had bigger openings and channels that would in turn help reduce the mass transfer resistance of the electrolyte through the oxide phase into the T-NT substrate beneath during the electrochemical tests (CV, charge−discharge, vide infra). This is obvious from the higher-magnification SEM images in Figure 3c′, compared to the compact oxide crystals obtained in Figure 3a′ and b′ corresponding to depositions at i = −1 and −3 mA cm^{-2}, respectively. Further increase in the deposition current density to −10 mA cm^{-2} resulted in a nonuniform-type deposit as shown in Figure 3d. Two different regions can be observed in this sample: oxide crystal agglomerations in some locations (Figure 3d′) and regions with scarcely distributed oxide phase (Figure 3d″). It is worth noting here that the further increase in deposition current density (−15 mA cm^{-2}) caused instability

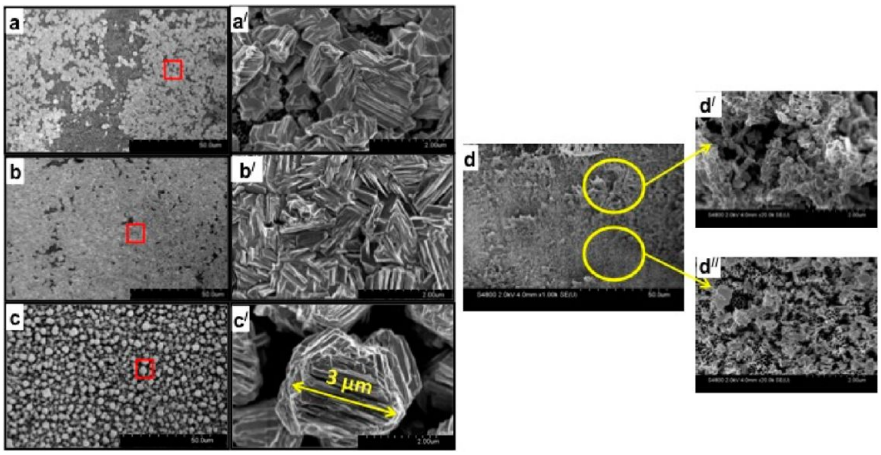

Figure 3. SEM image of the morphologies of the Bi_2O_3 deposit formed at (a) −1 m A cm^{-2}, (b) −3 mA cm^{-2}, (c) −5 mA cm^{-2}, and (d) −10 mA cm^{-2} for 15 min of deposition. The magnified images of the selected areas in these images are shown in corresponding images named as a′ through d″.

and delamination of the oxide layer during subsequent electrochemical experiments.

To evaluate the effect of deposition time on the morphology of the oxide, T-NT/Bi_2O_3 composites were prepared at a constant current density for various amounts of time. Since the deposition at $i = -5$ mA cm^{-2} produced the most uniform deposit, further deposition was performed at this current density for varied time periods of 5, 30, 45, and 60 min. Figure 4 shows the low- and high-magnification SEM images of the

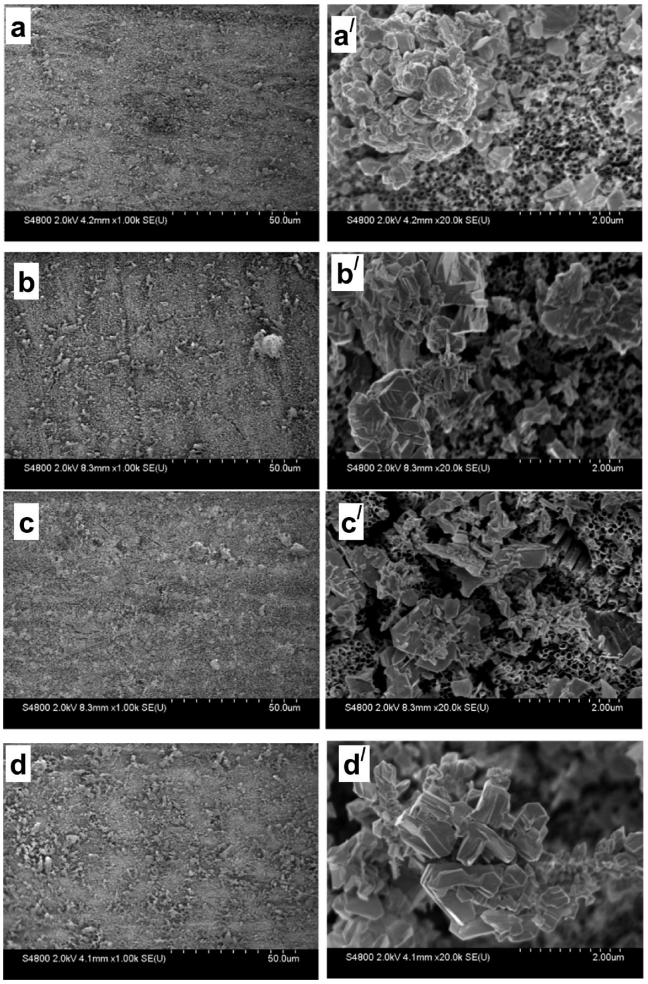

Figure 4. SEM image of the morphologies of the Bi_2O_3 deposit formed at $i = -5$ mA cm^{-2} for (a) 5 min, (b) 30 min, (c) 45 min, and (d) 60 min of deposition. The magnified images for each condition are shown in the corresponding images named as a′ through d′.

deposits obtained after various deposition times. When comparing these micrographs with that obtained after 15 min of deposition at the same current density (Figure 3c and c′), the underlying differences of the morphological aspects of the deposits can clearly be observed. For deposition times of 5, 30, 45, and 60 min, two specific regions were observed: (i) locations with Bi_2O_3 deposits that agglomerated into uneven size clusters and (ii) locations with scarcely distributed Bi_2O_3 crystals. The magnified images in Figure 4(a′−d′) indicated clearly these two regions. In fact, the morphology of the oxide formed at these deposition times was actually similar to that formed after 15 min of deposition at $i = -10$ mA cm^{-2} (Figure 3d). However, the volume fraction of the oxide agglomerates was much higher in the latter case. This may be partly attributed to the relatively higher deposition current density. The oxide agglomerations also seemed to have increased when the deposition time was increased from 5 to 60 min (Figure 4a−d). It is interesting to note that such agglomeration and scarce distribution did not occur when deposition was done for 15 min. The deposition was rather uniform with equiaxed crystals of the oxide phase as discussed above (Figure 3c and c′). From this detailed investigation on the effect of current density and time on deposition behavior, it can be concluded that, in this scope of experimentations, deposition at −5 mA cm^{-2} for 15 min would be preferred from the morphological standpoint. The nature of how the deposition occurs and leads to a particular morphology (equiaxed, unequiaxed, or random crystals) in this particular case of deposition is rather complicated and requires future investigations. Nevertheless, the growth of Bi_2O_3 may be preferential based on energetically favorable sites of the substrate under specific current density as well as time conditions applied during galvanostatic electrodeposition. In fact, the later discussions on the electrochemical performance (CV, charge−discharge) also demonstrated that the electrochemical properties obtained in this sample appeared to be optimal among the conditions examined.

The XRD analysis was carried out on the T-NT/Bi_2O_3 composite sample prepared at $i = -5$ mA cm^{-2} for 15 min. Figure 5 shows the XRD profile of the composite sample along

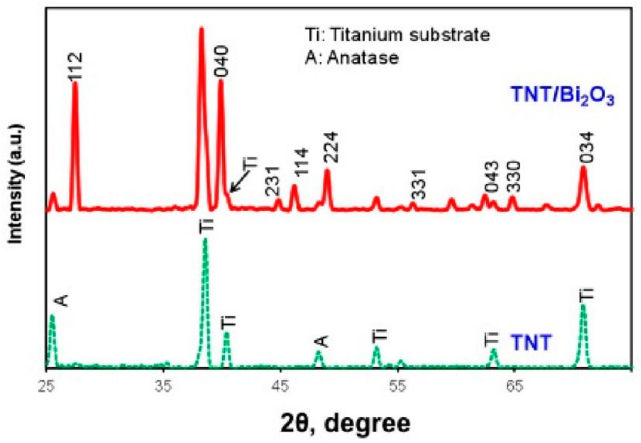

Figure 5. XRD profiles for the T-NT and T-NT/Bi_2O_3 composite prepared at $i = -5$ mA cm^{-2} for 15 min.

with that obtained for the bare T-NT. Clearly, the peaks from the crystallographic planes of (112), (040), (231), (114), (224), (331), (043), (330), and (034) observed in the T-NT/Bi_2O_3 sample suggested the formation of predominantly polycrystalline monoclinic α-Bi_2O_3 phase.[20] Some of the peaks pertaining to the anatase phase of the T-NT substrate can also be observed in the T-NT/Bi_2O_3 sample. The wide scan XPS spectrum of the same T-NT/Bi_2O_3 composite sample is shown in Figure 6a. It can be observed that the deposit mainly consists of Bi_2O_3. The carbon peak, observed in the spectrum, may be due to the contamination. Figure 6b shows the O 1s peak at a binding energy of about 530 eV. The two asymmetrical main peaks observed at 158.58 and 163.88 eV in Figure 6c correspond to the Bi $4f_{7/2}$ and $4f_{5/2}$ signals, respectively. These peaks suggest that the bismuth is present in the Bi^{3+} oxidation state, consistent with previous findings.[28] Two other small peaks can also be noticed in the spectrum in Figure 6c, corresponding to binding energies of 156.45 and

dx.doi.org/10.1021/am302738r | ACS Appl. Mater. Interfaces 2013, 5, 1688−1697

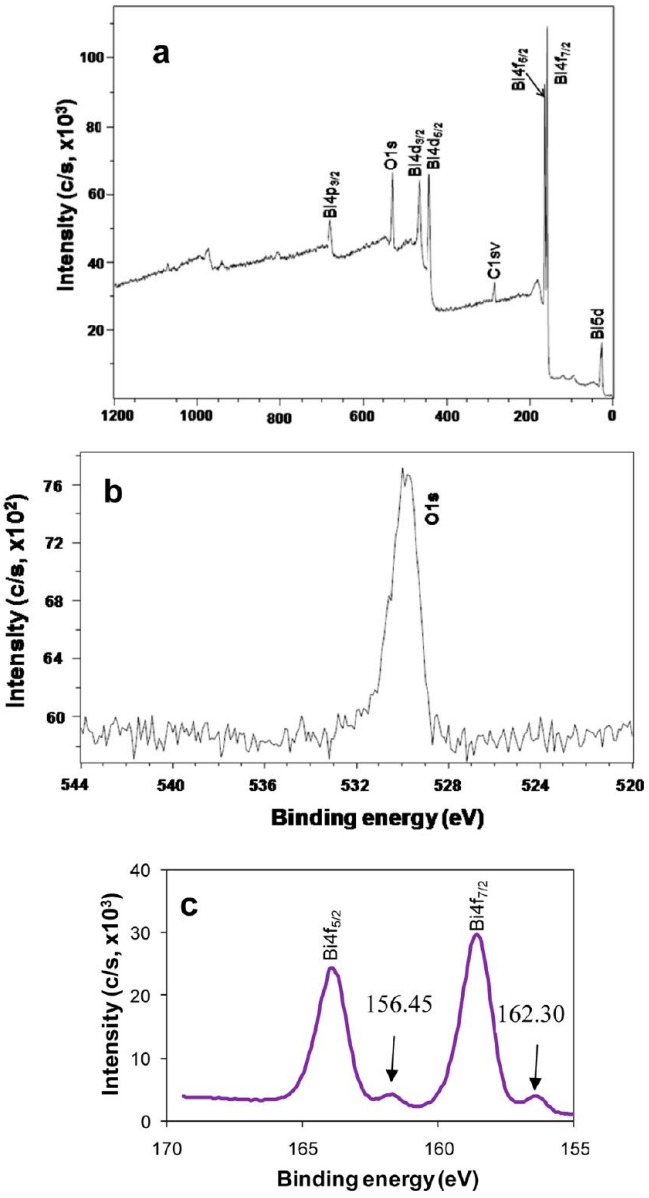

Figure 6. (a) XPS survey spectra for the T-NT/Bi_2O_3 composite prepared at $i = -5$ mA cm^{-2} for 15 min, (b) spectra for O 1s, and (c) Bi 4f photoelectron spectra together with small peaks for Bi metal at 156.45 and 162.30 eV.

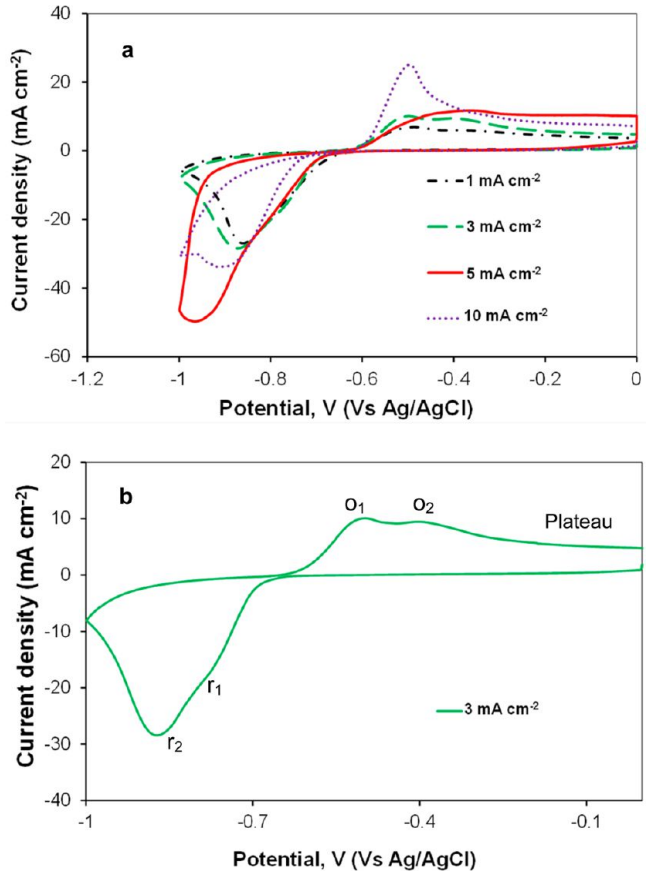

Figure 7. (a) CV profiles of various T-NT/Bi_2O_3 composites deposited at various current densities at a scan rate of 100 mV s^{-1}. (b) The CV profile of the composite material prepared at $i = -3$ mA cm^{-2} at 100 mV s^{-1} with all redox peaks marked distinctly.

162.30 eV. These peaks agree with the Bi 4f signals for Bi metal,[29] indicating the presence of a small amount of metallic Bi in the oxide layer.

The electrochemical behavior of the T-NT/Bi_2O_3 composites obtained after 15 min of deposition at various current densities were evaluated by CV technique. The CV was performed at a scan rate of 100 mV s^{-1}, and the resultant curves are presented in Figure 7a. Two sets of redox peaks were observed in the CV profiles of the composite samples. The presence of these redox peaks suggested that the capacitance of the composite electrodes was mainly due to the rapid and reversible faradic reactions on the electrode/electrolyte interface. Also, the cathodic current peak increased gradually with increasing deposition current density from -1 to -5 mA cm^{-2}. However, a further increase in deposition current density to -10 mA cm^{-2} caused a decrease in cathodic current density. The highest cathodic current was obtained for the T-NT/Bi_2O_3 composite electrode prepared at $i = -5$ mA cm^{-2} for 15 min, which is also consistent with the desirable oxide morphology obtained in this sample (Figure 3c). The equiaxed crystals facilitated larger channels for the electrolyte penetration in this sample, which may not be feasible in the other samples due to the compact oxide layer morphology. The anodic current peaks in the CV also increased with an increase in deposition current densities for the oxide phase.

The interaction of Bi_2O_3 with hydroxide-based electrolyte during CV analysis resulted in two sets of redox peaks. For a better visual, the CV curve obtained at the scan rate of 100 mV s^{-1} for the composite electrode deposited at $i = -3$ mA cm^{-2} for 15 min is shown in Figure 7(b) where redox peaks are clearly marked. This phenomenon has also been reported in previous works.[23−25] The redox behavior of Bi_2O_3 in 1 M KOH solution had been studied in detail using a CV technique.[30] The study indicated that the reduction process for the Bi_2O_3 in OH^- containing solution is initiated by partial dissolution of the oxide to the BiO^- ionic species. The two reduction peaks at r_1 and r_2 correspond to the reduction of Bi(III) to Bi metal. However, the current peak at r_1 is small because a small amount of adsorbed BiO^- ions reduce to Bi through the following reactions[30]

$$BiO_2^- \rightarrow BiO_{2(ads)}^- \quad (3)$$

$$BiO_{2(ads)}^- + e^- \rightarrow BiO_{2(ads)}^{2-} \quad (4)$$

dx.doi.org/10.1021/am302738r | ACS Appl. Mater. Interfaces 2013, 5, 1688−1697

$$2H_2O + 3BiO_{2(ads)}^{2-} \xleftrightarrow{\text{disproportionation}} 2BiO_{2(ads)}^{-} + 4OH^- + Bi_{ads}^{0} \quad (5)$$

$$Bi_{ads}^{0} \rightarrow Bi_{metal} \quad (6)$$

The majority of the BiO^- ions are in the dissolved state, which undergoes the following reactions to form metallic Bi which corresponds to the larger reduction peak at r_2

$$BiO_2^- + e^- \rightarrow BiO_2^{2-} \quad (7)$$

$$2H_2O + 3BiO_2^{2-} \xleftrightarrow{\text{disproportionation}} 2BiO_2^- + 4OH^- + Bi^0 \quad (8)$$

$$Bi^0 \rightarrow Bi \quad (9)$$

The oxidation peaks at O_1 and O_2, and the plateau, as shown in Figure 7b, are related to the oxidation of Bi metal to Bi_2O_3. The peak at O_1 can be attributed to a small amount of Bi metal sites located near the Bi-metal/solution interface.[30] However, the general reaction pathway for the oxidation processes for the two peaks are the same as outlined by the following equations

$$Bi_{metal} \rightarrow Bi^+ + e^- \quad (10)$$

$$3Bi^+ \xleftrightarrow{\text{disproportionation}} Bi^{3+} + 2Bi_{metal} \quad (11)$$

$$3OH^- + Bi^{3+} \rightarrow Bi(OH)_3 \quad (12)$$

$$Bi(OH)_3 \rightarrow BiOOH + H_2O \quad (13)$$

To study the effect of deposition time on the CV performance of the composite materials, Bi_2O_3 was deposited on to the T-NT substrates for 5, 15, 30, 45, and 60 min at $i = -5$ mA cm^{-2}. Figure 8a shows the CV profiles for the T-NT/Bi_2O_3 electrodes deposited for various amount of times. The current–voltage response of the CV profiles for the samples are consistent with the corresponding oxide morphologies obtained in these deposition conditions (Figure 4). The agglomerated and nonuniformly distributed Bi_2O_3 oxides in the 5, 30, 45, and 60 min samples showed lower current values compared to that of the 15 min samples. This is again consistent with respect to the uniform oxide morphology observed in the 15 min sample as discussed above.

To study the effect of voltage scan rate on the electrochemical capacitance performance of the composite materials, CV analysis was also performed at several scan rates on the sample prepared at $i = -5$ mA cm^{-2} for 15 min. The CV profiles recorded at 20, 50, 100, and 200 mV s^{-1} scan rates are shown in Figure 8b. The anodic and cathodic current increased with the increase in the scan rate, suggesting good capacitative response of the electrode material. On the basis of the integrated area under the CV curve, the interfacial capacitance of the electrode material was calculated as

$$C = \frac{Q}{VA} \quad (14)$$

where Q is the total charge from the integrated area of the CV profile; V is the voltage window; and A is the area of the electrode in contact with the electrolyte. Determination of interfacial capacitance of the electrode using eq 14 showed a decrease in capacitance with the increase in scan rate. The values for interfacial capacitance were 185, 170, 122, and 50 mF cm^{-2} at scan rates of 20, 50, 100, and 200 mV s^{-1}, respectively.

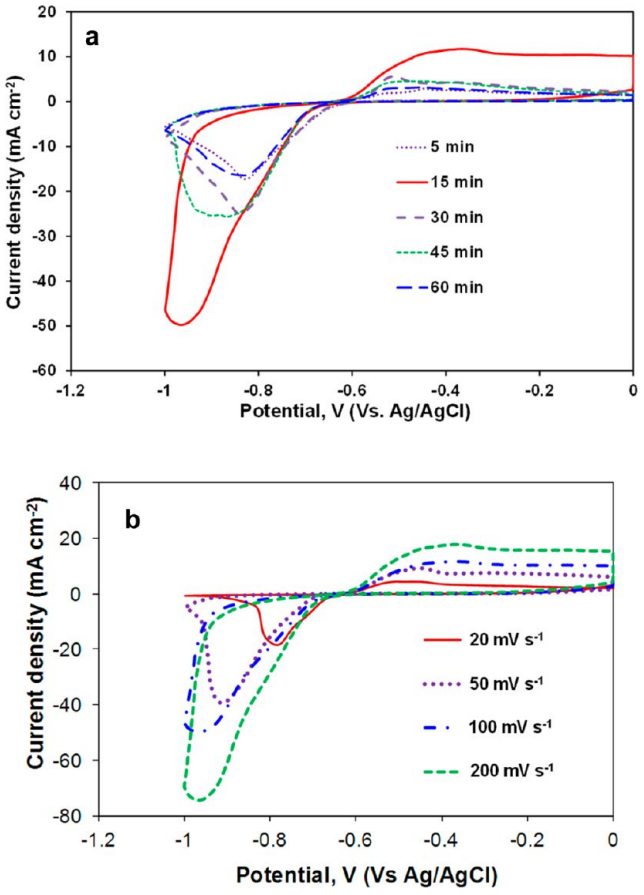

Figure 8. (a) CV profiles recorded at a scan rate of 100 mV s^{-1} for various T-NT/Bi_2O_3 composites deposited at $i = -5$ mA cm^{-2} for 5 to 60 min. (b) The CV profile for the composite material deposited at $i = -5$ mA cm^{-2} for 15 min at increasing scan rates.

A similar decreasing trend of interfacial capacitance was also observed in the Cu/Bi_2O_3 composite electrode upon an increase in the scan rate from 20 to 200 mV s^{-1}.[20] It was suggested that the decrease in capacitance was primarily because of the inner active sites in the oxide layer that are not readily accessible by the electrolyte at higher scan rates due to diffusion limitations. Therefore, a sustainable redox transition was not complete with an increase in scan rate of the potential, leading to a decrease in the interfacial capacitance.

The stability of the T-NT/Bi_2O_3 composite electrode was also evaluated by employing consecutive CV cycles up to 500 cycles at a scan rate of 100 mV s^{-1}. The composite electrode prepared at $i = -5$ mA cm^{-2} for 15 min was used for the analysis. Figure 9 shows the CV plots for the 1st, 50th, and 100th cycles, while the inset figure shows the comparison of CV plots after the 100th and 500th cycles. It appears that the specific capacitance decreased slowly till 100 cycles and stabilized thereafter up to the 500th cycle.

The galvanostatic charge–discharge behavior of various T-NT/Bi_2O_3 composite electrodes was evaluated at a constant current density of 1 mA cm^{-2} in the voltage window of 0 to −1 V. Figure 10 shows the charge–discharge profiles for composite electrodes prepared at i: −1, −3, −5, and −10 mA cm^{-2} for 15 min. The profiles, in terms of voltage–time (V–t), appeared to be nonsymmetric with an associated IR drop. The discharge curves consisted of two parts: (i) a steep voltage drop due to the internal resistance and (ii) a curved part with gradual

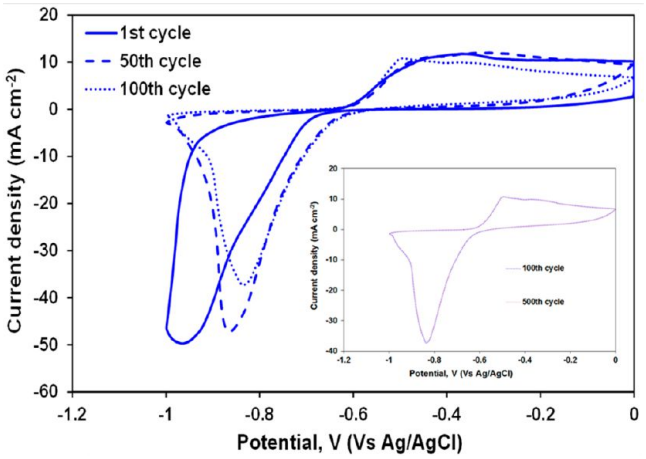

Figure 9. 1st , 50th, and 100th CV profiles recorded at a scan rate of 100 mV s^{-1} for the T-NT/Bi_2O_3 composite prepared at $i = -5$ mA cm^{-2} for 15 min. The inset shows the CVs after the 100th and 500th scan, showing no change in the current response (very stable).

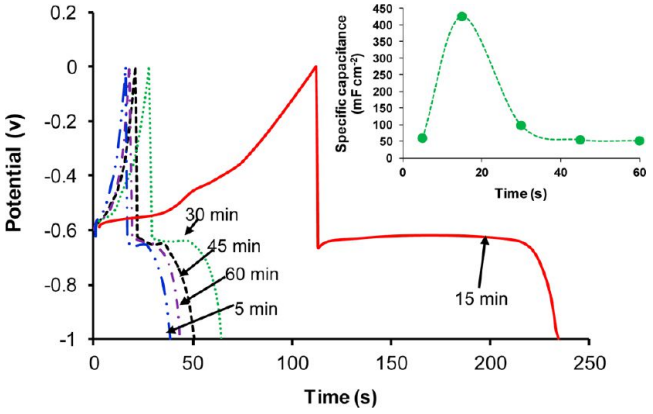

Figure 11. Galvanostatic $V-t$ profiles carried out at the current density of 1 mA cm^{-2} for the T-NT/Bi_2O_3 composite prepared at $i = -5$ mA cm^{-2} for various amounts of time. The inset illustrates the change in the interfacial capacitance of the composite electrodes with the increase in deposition time.

decrease in voltage due to the change in energy within the capacitor. Using the following relationship, the interfacial capacitance of the electrode materials was calculated

$$C = \frac{It}{\Delta VA} \tag{15}$$

where I is the charge−discharge current density; t is the time obtained from the $V-t$ plots; ΔV is the voltage window; and A is the area of the electrode. The calculated interfacial capacitance of the electrodes was plotted as a function of the deposition current density and shown in the inset of Figure 11. It can be observed that the highest interfacial capacitance (~430 mF cm^{-2}) was obtained for the sample prepared at $i = -5$ mA cm^{-2} for 15 min, which was ~94% higher than that obtained at $i = -10$ mA cm^{-2}. This result is in agreement with the CV analysis (Figure 7a) and the morphology of the oxide formed in this deposition condition (Figure 3c).

The charge−discharge experiments were also carried out for the composite samples prepared at $i = -5$ mA cm^{-2} for a varied amount of times. The resultant $V-t$ curves are plotted in Figure 11. Similar charge−discharge behavior as described above was obtained in terms of the shape of the charge−discharge profiles (the discharge curve consisted of two parts vide supra). The calculated interfacial capacitance of the composite electrodes (eq 15) is shown as a function of the deposition times in the inset of Figure 11. As expected from our previous analysis of CV experiments (Figure 8a) and the morphology of the oxides (Figures 3 and 4), samples prepared at $i = -5$ mA cm^{-2} for 15 min outperformed all other conditions. For example, the increase in interfacial capacitance for this sample was more than 300% that of the sample deposited for 30 min at the same

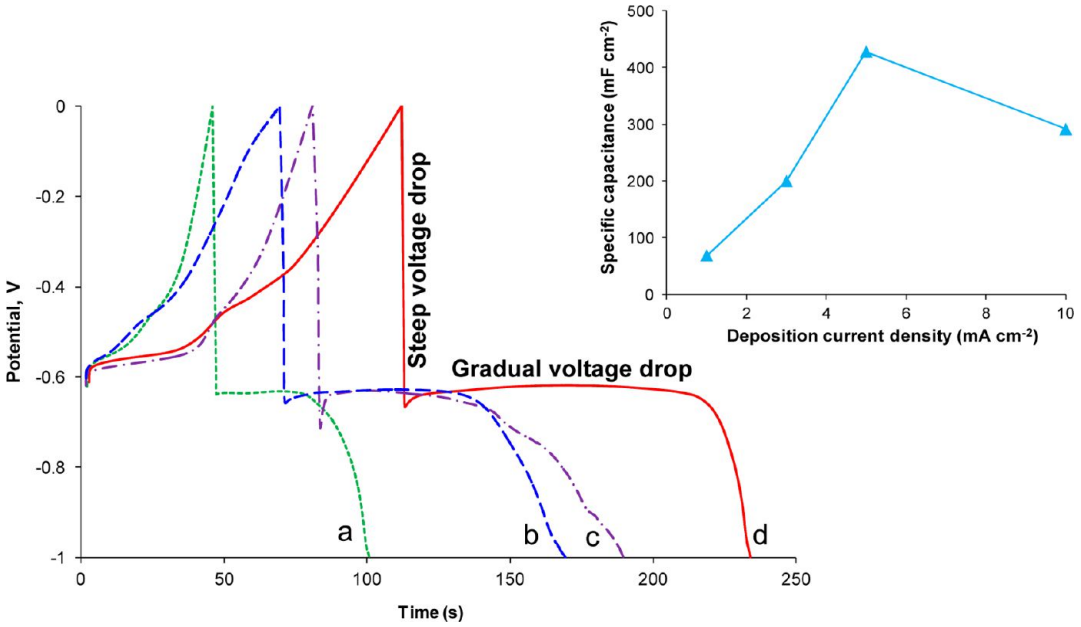

Figure 10. Galvanostatic $V-t$ profiles carried out at the current density of 1 mA cm^{-2} for T-NT/Bi_2O_3 composites deposited at current densities of (a) −1 mA cm^{-2}, (b) −3 mA cm^{-2}, (c) −10 mA cm^{-2}, and (d) −5 mA cm^{-2} for 15 min. The inset shows the variations of the interfacial capacitance of the composite electrodes with the deposition current density.

current density. Therefore, it would be reasonable to suggest that among various conditions investigated in terms of deposition current densities and times the best result was obtained when deposition was done for 15 min at $i = -5$ mA cm^{-2}.

Further galvanostatic charge–discharge experiments were conducted at current densities of 3 and 5 mA cm^{-2} for the sample prepared at $i = -5$ mA cm^{-2} for 15 min to investigate the effect of an increase in charge–discharge current densities on capacitative performance of the electrode. Figure 12a shows

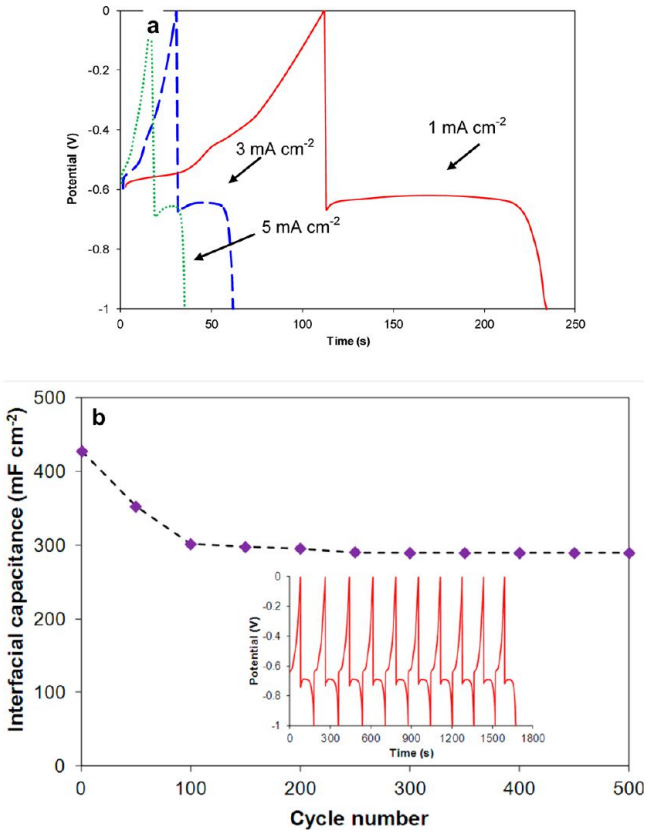

Figure 12. (a) Galvanostatic $V-t$ profiles carried out at the current densities of 1, 3, and 5 mA cm^{-2} for T-NT/Bi_2O_3 composites prepared at $i = -5$ mA cm^{-2} for 15 min. (b) Variations in interfacial capacitance of the T-NT/Bi_2O_3 composites deposited at $i = -5$ mA cm^{-2} for 15 min with cycle number. The inset shows the first 10 cycles of representative $V-t$ curves for the same composite sample.

the $V-t$ responses. It can be observed that the interfacial capacitance decreased with an increase in charge–discharge current density, as one would expect.[3] The interfacial capacitance at the imposed current densities of 3 and 5 mA cm^{-2} was approximately 340 and 325 mF cm^{-2}, which was 20 and 23% less compared to that obtained at 1 mA cm^{-2}, respectively. The stability of the electrode was also evaluated by imposing continuous charge–discharge cycles up to 500 cycles on the T-NT/Bi_2O_3 composite sample (prepared at $i = -5$ mA cm^{-2} for 15 min) at a charge–discharge current density of 1 mA cm^{-2}. Figure 12b shows the interfacial capacitance of the electrode as the function of cycle number. Consistent with the CV results (Figure 9), the capacitance decreased gradually for the first 100 cycles—the decrease being about 25% of that obtained at the beginning of the cycle. After that, the capacitance performance of the electrode appeared to be stable. Capacitance retention of approximately 75% was achieved in the composite material. The inset in Figure 12b shows representative charge–discharge cycles from the experiment, illustrating the stable nature of the electrode. High interfacial capacitance and excellent cycle stability are key parameters to any electrochemical capacitor, both of which are found to be exhibited well by our composite material. The SEM micrograph of the composite electrode after 500 cycles of charge–discharge is shown in Figure 13. It can be observed that

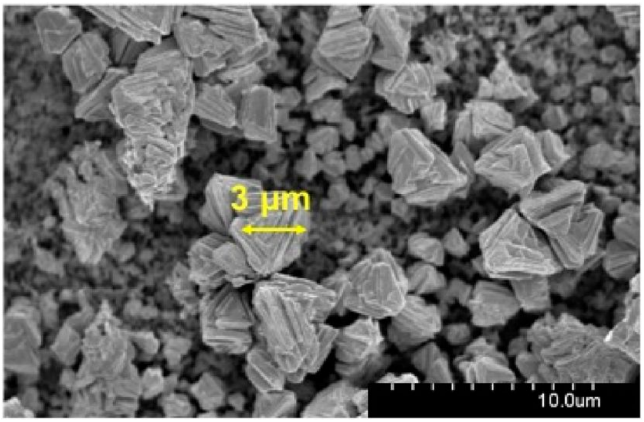

Figure 13. SEM image of the T-NT/Bi_2O_3 composites prepared at $i = -5$ mA cm^{-2} for 15 min after 500 galvanostatic charge–discharge cycles.

the deposited oxide crystals were intact in terms of their shapes, sizes, and distributions even after undergoing such high charge–discharge cycles. For example, the average sizes of the oxide crystals were ~3 μm before and after the charge–discharge test (Figure 13 and Figure 3c′).

The interfacial capacitance values reported in the literature for several electrode materials are compiled in Table 1 together with that obtained in our study. The table summarizes the synthesis method for the electrode materials, the electrolyte, and the potential window used for capacitance study and the interfacial capacitance achieved therein. The enhanced capacitance obtained in our work as well as the large operating potential window (1.0 V) suggested that the T-NT/Bi_2O_3 composite material has the potential to be used in supercapacitor applications.

4. CONCLUSION

In the study, we have reported a simple and optimized electrodeposition technique to synthesize a titania nanotube array (T-NT)/bismuth oxide (Bi_2O_3) composite material for supercapacitor applications. The shape, morphology, and the distributions of the Bi_2O_3 deposits were highly sensitive to the deposition parameters, specifically the deposition current density and time. The morphology and crystal phases present in the deposited oxides were analyzed using various characterization tools, such as SEM, XRD, and XPS. The electrochemical tests on the composite materials were carried out in 1 M NaOH aqueous solution using a three-electrode experimental setup. The CV analysis demonstrated that the capacitance of the composite materials emanated from the fast and reversible faradic-redox reactions occurring in the electrode/electrolyte interface. To validate the results obtained by CV, galvanostatic charge–discharge experiments were also carried out on the electrode materials. The results in fact confirm the findings of

Table 1. Comparison of Interfacial Capacitance of Various Electrode Materials As Reported in the Literature with That Obtained in This Study

electrode	synthesis method	electrolyte	potential window (ΔV)	interfacial capacitance (mF cm^{-2})
TiO_2 nanotube[31]	Electrochemical anodization	1 M KCl	0.8	~0.02−0.9
Ti-18 V nanotube[32]	Electrochemical anodization of Ti-18 wt % V alloy	0.1 M $HClO_4$	0.8	~20
Ti−Ni nanotube[33]	Electrochemical anodization of Ti-56 wt % Ni alloy	1 M KOH	0.5	~2.8
NiO nanoparticle film[33]	Using a organic paste via doctor blade process	1 M KOH	0.5	~2.8
Tungsten oxide nanoraod on Al/W/Ti substrate[34]	Two-step anodization process	1 M Na_2SO_4	1.0	~2.8
Fe_2O_3 thin film[35]	SILAR method	1 M NaOH	0.7	~120
TiO_2 nantube/NiO composite[3]	Electrodepositon of NiO on the TiO_2 nanotube	1 M NaOH	0.5	~128
Coaxial NiO/Ni nanowire[9]	Electrodeposition of Ni on alumina template and subsequent plasma annealing in oxygen	1 M KOH	0.5	~360
C/MnO_2 composite[36]	Potentiostatic deposition of MnO_2 on carbon substrate	2 M KCl	1.0	~288
Ti/IrO_2 composite[37]	Thermal decomposition of IrO_2 on Ti substrate	0.5 M H_2SO_4	1.0	~53
Stainless steel/RuO_2 composite[38]	Potentiostatic electrodeposition	0.5 M H_2SO_4	0.7	~452
Bi_2O_3/Cu composite[20]	Electrodeposition of Bi_2O_3 on Cu	1 M NaOH	0.8	~22
TNT/Bi_2O_3 composite [present study]	Electrodeposition of Bi_2O_3 on TiO_2 nanotube arrays	1 M NaOH	1.0	~427

the CV analysis, suggesting that the interfacial capacitance of the composite materials can reach very high values (~430 mF cm^{-2}) upon optimization of the shape and size distribution of the oxide phases on the nanotubular substrate. This high value was attained because of the combined effect of the redox reactions associated with the Bi_2O_3 in the presence of the electrolyte as well as the high surface area associated with the nanotubular nature of the substrate material. The stability of the composite material was also evaluated by employing continuous charge−discharge cycles up to 500 cycles. A very high percentage (~75%) of capacitance retention was achieved in the composite material. Lastly, the interfacial capacitance obtained in this work was compared with the previously reported literature values for various other electrode materials to elucidate the superior behavior of the T-NT/Bi_2O_3 composite synthesized in this work.

■ ASSOCIATED CONTENT

Supporting Information

Figures: (S1) Comparison of CV profiles of bare T-NT and T-NT/Bi_2O_3 composite prepared at $i = -5$ mA cm^{-2} for 15 min, (S2) Comparison of CV profiles of bare Ti/Bi_2O_3 and T-NT/Bi_2O_3 composites. The deposition of Bi_2O_3 was performed at $i = -5$ mA cm^{-2} for 15 min, (S3) Raman profiles of bare T-NT and T-NT/Bi_2O_3 composite prepared at $i = -5$ mA cm^{-2} for 15 min. This material is available free of charge via the Internet at http://pubs.acs.org.

■ AUTHOR INFORMATION

Corresponding Author

*E-mail: mano.misra@utah.edu.

Notes

The authors declare no competing financial interest.

■ ACKNOWLEDGMENTS

The U.S. Department of Energy (DE-FC-36-06GO86066) supported the work presented here.

■ REFERENCES

(1) Conway, B.E. *Electrochemical Supercapacitors: Scientific Fundamentals and Technological Applications*; Kluwer Academic/Plenum Press: New York, 1999.
(2) Babakhani, B.; Ivey, D. G. *J. Power Sources* **2010**, *195*, 2110−2117.
(3) Xie, Y.; Zhou, L.; Huang, C.; Huang, H.; Lu, J. *Electrochim. Acta* **2008**, *53*, 3643−3649.
(4) Jow, T.R.; Zheng, J.P. *J. Electrochem. Soc.* **1998**, *145*, 49−52.
(5) Reddy, R.N.; Reddy, R.G. *J. Power Sources* **2004**, *132*, 309−314.
(6) Zhao, G.Y.; Xu, C.L.; Li, H.L. *J. Power Sources* **2007**, *163*, 1132−1136.
(7) Prasad, K.R.; Miura, N. *Appl. Phys. Lett.* **2004**, *85*, 4199−4202.
(8) Hu, C.-C; Cheng, C.-Y. *Electrochem. Solid State* **2002**, *5*, A43−A46.
(9) Hasan, M.; Jamal, M.; Razeeb, K. M. *Electrochim. Acta* **2012**, *60*, 193−200.
(10) Xu, J.; Gao, L.; Cao, J.; Wang, W.; Chen, Z. *Electrochim. Acta* **2010**, *56*, 732−736.
(11) Lin, C.-C.; Chen, H. −W. *Electrochim. Acta* **2009**, *54*, 3073−3077.
(12) Wang, G.; Zhang, L.; Kim, J.; Zhang, J. *J. Power Sources* **2012**, *217*, 554−561.
(13) Wang, Y.J.; Zhang, X.G. *J. Electrochem. Soc.* **2005**, *152*, A671−A676.
(14) Fu, Y.; Wei, Z. D.; Chen, S. G.; Li, L.; Feng, Y. C.; Wang, Y. Q.; Ma, X. L.; Liao, M. J.; Shen, P. K.; Jiang, S.P. *J. Power Sources* **2009**, *189*, 982−987.
(15) Benoit, A.; Paramasivam, I.; Nah, Y. -C.; Roy, P.; Schmuki, P. *Electrochem. Commun.* **2009**, *11*, 728−732.
(16) Sarma, B.; Smith, Y.R.; Mohanty, S.K.; Misra, M. *Mater. Lett.* **2012**, *85*, 33−35.
(17) Smith, Y.R.; Sarma, B.; Mohanty, S.K.; Misra, M. *Electrochem. Commun.* **2012**, *19*, 131−133.
(18) Smith, Y.R.; Sarma, B.; Mohanty, S.K.; Misra, M. *ACS Appl. Mater. Interfaces* **2012**, *4*, 5883−5890.
(19) Misra, M.; Raja, K.S. *On Solar Hydrogen & Nanotechnology*; Vayssieres, L., Ed.; John Wiley & Sons: Chichester, UK, 2010; Vol. *1*, pp 266−290.
(20) Gujar, T.P.; Shinde, V.R.; Lokhande, C.D.; Han, S. −H. *J. Power Sources* **2006**, *161*, 1479−1485.
(21) Ding, S.; Shan, D.; Xue, H.; Cosnier, S. *Bioelectrochemistry* **2010**, *79*, 218−222.
(22) Gujar, T.P.; Shinde, V.R.; Lokhande, C.D.; Mane, R. S.; Han, S. −H. *Appl. Surf. Sci.* **2005**, *250*, 161−167.
(23) Xia, N.; Yuan, D.; Zhou, T.; Chen, J.; Mo, S.; Liu, Y. *Mater. Res. Bull.* **2011**, *46*, 687−691.
(24) Yuan, D.S.; Zeng, J. H.; Kristian, N.; Wang, Y.; Wang, X. *Electrochem. Commun.* **2009**, *11*, 313−315.

(25) Wang, H. -W.; Hu, Z. -A.; Chang, Y. -Q.; Chen, Y. -L.; Lei, Z. -Q.; Zhang, Z. -Y.; Yang, Y. -Y. *Electrochim. Acta* **2010**, *55*, 8974−8980.
(26) Murugesan, M.; Smith, Y.R.; Subramanian, V. *J. Phys. Chem. Lett.* **2010**, *1*, 1631−1636.
(27) Huang, X.; Yan, J.; Zeng, F.; Yuan, X.; Zou, W.; Yuan, D. *Mater. Lett.* **2013**, *90*, 90−92.
(28) Xiaohong, W.; Wei, Q.; Weidong, H. *J. Mol. Catal. A: Chem.* **2007**, *261*, 167−171.
(29) Hwang, G. H. *Sens. Actuators B: Chem.* **2008**, *135*, 309−316.
(30) Vivier, V.; Regis, A.; Sagon, G.; Nedelec, J. −Y.; Yu, L.T.; Vivier, C. C. *Electrochim. Acta* **2001**, *46*, 907−914.
(31) Salari, M.; Konstantinov, K.; Liu, H.K. *J. Mater. Chem.* **2011**, *21*, 5128−5133.
(32) Yang, Y.; Kim, D.; Yang, M.; Schmuki, P. *Chem. Commun.* **2011**, *47*, 7746−7748.
(33) Kim, J. −H.; Zhu, K.; Yan, Y.; Perkins, C. L.; Frank, A.J. *Nano Lett.* **2010**, *10*, 4099−4104.
(34) Park, S.H.; Kim, Y.H.; Lee, T.G.; Shon, H.K.; Park, H.M.; Song, J.Y. *Mater. Res. Bull.* **2012**, *47*, 3612−3618.
(35) Kulal, P.M.; Dulal, D.P.; Lokhande, C.D.; Fulari, V.L. *J. Alloy Compd.* **2011**, *509*, 2567−2571.
(36) Chang, J.-K.; Tsai, T.W. *J. Electrochem. Soc.* **2003**, A1333−A1338.
(37) Grupioni, A.A.F.; Arashiro, A.; Lassali, T.A.F. *Electrochim. Acta* **2002**, *48*, 407−418.
(38) Patake, V.D.; Pawar, S.M.; Shinde, V.R.; Gujar, T.P.; Lokhande, C.D. *Curr. Appl. Phys.* **2010**, *10*, 99−103.